Chapter 8

# Mapping of Ground Deformations with Interferometric Stacking Techniques

Paolo Pasquali, Alessio Cantone, Paolo Riccardi,
Marco Defilippi, Fumitaka Ogushi,
Stefano Gagliano and Masayuki Tamura

Additional information is available at the end of the chapter

http://dx.doi.org/10.5772/58225

## 1. Introduction

Interferometric stacking techniques emerged in the last decade as methods to obtain very precise measurements of terrain displacements, and especially of subsidence phenomena. In particular, the so-called Persistent Scatterers [1] and Small BASeline [2] methods can be considered as the two most representative stacking approaches.

In both cases, the exploitation of 20 or more satellite Synthetic Aperture Radar (SAR) acquisitions obtained from the same satellite sensor with similar geometries on the interest area allows to measure displacements with an accuracy in the order of a few mm / year, and to derive the full location history of "good" pixels with an accuracy of 1cm or better for every available date.

This chapter is presenting an extensive analysis of the two methods, a validation of the results obtained in same geographical areas with the different techniques and an evaluation of the suitability of these techniques for different applications.

All results shown in this chapter have been generated with the SARscape® software package.

## 2. Interferometric stacking techniques

While trying to provide an answer to the same problem, i.e. how to measure small land displacements out of a series of SAR images acquired on a same geographical area under a

same geometry, the PS and SBAS approaches designed two algorithms that focus each on a different type of objects and land cover to favour in the analysis: the PS technique focuses on so-called Point Targets, i.e. objects possibly of small size and with a very well characterized geometry like corner reflectors (e.g. buildings, rocks) and with a high temporal stability of the backscattered signal; the SBAS technique vice-versa is concentrating the analysis on so-called distributed targets, like open fields and not very geometrically characterized objects. Both approaches, exploiting a reference Digital Elevation Model in input of the workflow, also estimate its errors as residual height component together with the displacement series.

As shown in Figure 1 on the left, the original PS approach is selecting one of the images of the input stack as reference and generating all differential interferograms between this and the other acquisitions. Focusing on Point Targets, no limits of critical baseline shall be considered, and no spectral shift or other filtering are performed [3]; the algorithm is then operating on the phase time series of each of the pixels separately, without performing any phase unwrapping. Both these features allow to obtain the maximum spatial resolution of the final results i.e. total independency of the measures for adjacent pixels, as well as eliminate the possibility of unwrapping errors propagation.

The estimation of the average linear displacement rate and of the residual height correction factor is performed through a kind of frequency analysis: a range of linear displacement rates and of residual heights is explored and, for each of the explored values, the phase trend corresponding to the tested values is subtracted from the measured phase time series, and a so-called *temporal coherence* is estimated by normalising the summation of the de-trended complex time series.

This analysis is in the original algorithm performed on selected pixels (*PS candidates*) that show no significant variations of the backscatter amplitude over the time; in any case, only pixels showing high values of the temporal coherence are finally considered as true PSs.

It shall be noticed that the temporal coherence should more appropriately be considered as a measure of linearity of the phase time series; points characterised by stable radar backscatter and very low phase noise and temporal decorrelation, but characterised by significantly non-linear displacement regimes will not be recognised as PSs by such analysis.

Being the PS estimation performed independently on each pixel, large variations of phase from one date to the next in the time series due to large displacements or irregular temporal sampling will also make the analysis difficult, resulting in such cases in wrong estimations of the displacement rates and / or difficulties in the identification of the corresponding PSs.

The SBAS approach, as shown in Figure 1 on the right, is generating all differential interferograms from the input images stack that fulfil criteria of temporal and geometric baseline within a given interval in time or respectively normal baseline respect to the critical one. The second condition is trying to limit the impacts of volume decorrelation over natural distributed targets; to re-enforce this, spectral shift and adaptive filtering steps (typical of standard SAR interferometry) are included in the workflow.

The interferograms (coregistered on a common geometry) are then unwrapped, either with a conventional 2D (interferogram-by-interferogram) or with a combined 3D approach [4]. This

http://dx.doi.org/10.5772/58225

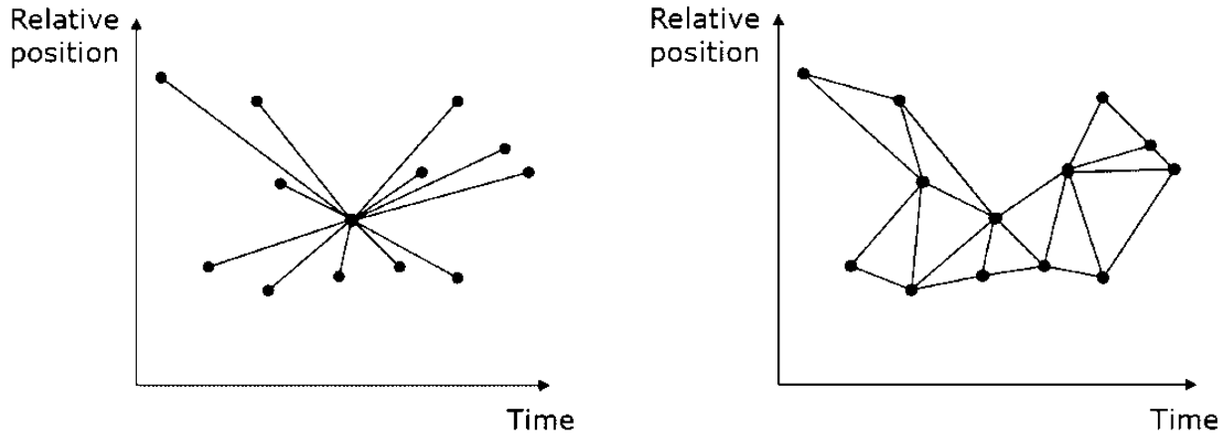


**Figure 1.** Typical processing schemes for the PS (on the left) and SBAS (on the right) techniques each circle corresponds to one acquisition, each connecting segment one interferogram.

step, surely the most challenging in SAR interferometry, relies on some spatial continuity of the interferometric phase, and hence is expecting some form of spatial correlation of the displacement phenomena happening in the region of interest, and it is a potential source of errors propagation. On the other side, this step makes the approach more robust toward irregular series and fast displacements.

The average displacement rate and the residual height correction factor are then estimated by inverting a linear system, possibly with a robust SVD approach, that includes all measures (one for each interferogram) together with their proportionality coefficients depending on the temporal and geometric baseline of each pair.

The final identification of reliable results is derived for example from the average (spatial) coherence of each pixel; no assumption is made in particular on the linearity of the true underlying displacement, and average displacement rates can also be estimated for pixels characterised by strongly non-linear behaviours, given that they remain coherent in most of the interferograms of the network.

Different models (e.g. quadratic or cubic) can be exploited during the inversion phase, and the reconstruction of the LMS time series of the displacements is also possible with this approach without the need of assuming any type of model for the true temporal deformation.

Both algorithms, after a first estimate of the average displacement rates and height correction factors, perform an estimated of the so-called "Atmospheric Phase Screen". The impact of atmospheric heterogeneities on the propagation of the SAR signal is considered as a spatially low frequency signal, with very short temporal correlation. Appropriate space – time filtering is performed on the phase time series after removing the results of the first estimate to evaluate the pixel-by-pixel and date-by-date impact of the APS and remove it from the original phase time series. A second and final iteration is then performed of the APS-corrected data with either of the PS or SBAS approaches to obtain a refined final estimate of the displacement rate and height correction.

As final step, the time series of the displacement for each pixel and date is obtained in both approaches.

A synthetic comparison of the characteristics of the two approaches is given in the following Table.

| PS | SBAS |
|---|---|
| Analyse independent, uncorrelated motions | Monitor at best spatially correlated motions |
| Expect pixel-wise continuous time series | Capable of handling time series with temporal holes |
| Time interval between two acquisitions limited by displacement rate | Time interval between two acquisitions limited by temporal decorrelation |
| Very accurate on PSs | Slightly less accurate |
| Linear displacements favoured | Larger variety of parametric models possible. Non-parametric modelling possible |

**Table 1.** Main characteristics from the exploitation point of view of the PS and SBAS approaches.

## 3. Factors affecting the final expected precision

As for standard interferometry, temporal decorrelation can be considered as the most important factor affecting the precision obtainable from the processing of an interferometric stack of SAR images.

An estimation of the expected precision of the measured displacements can be derived from the interferometric coherence. Known its value for a certain pixel, well known relationships [6] allow to obtain an estimate of the interferometric phase standard deviation, then scaled by the system wavelength to obtain a correspondent estimation of the expected displacement precision. By exploiting this approach, it is possible to evaluate for example which is the level of coherence necessary to obtain the same precision with a certain system wavelength as with another wavelength at a given coherence level, as shown in Figure 2.

Here a C-band system (as ERS-1/2, ENVISAT ASAR, Radarsat-1/2 and the forthcoming Sentinel-1) has been selected as reference: the red curve provides an estimate of the coherence level that is necessary, for every C-band coherence value, to obtain the same displacement precision with a L-band system (as PALSAR-1 and the forthcoming PALSAR-2), while the blue curve presents a similar comparison between a C-Band and a X-band (as COSMO-Skymed and TerraSAR-X / TanDEM-X) system.

It can here be seen how, assuming a minimum acceptable value of 0.2 for the C-Band coherence, comparable accuracies can be obtained from L-band measurements only for coherence levels of 0.6 or more. This corresponds to the L-band longer wavelength (if compared to C-band) and hence poorer displacement sensitivity.

http://dx.doi.org/10.5772/58225

On the other hand, as expected due to the shorter wavelength and hence better displacement sensitivity, X-band systems provide, with coherence 0.2, displacement precisions that are comparable with what can be obtained from a C-band system with coherence 0.4 or more.

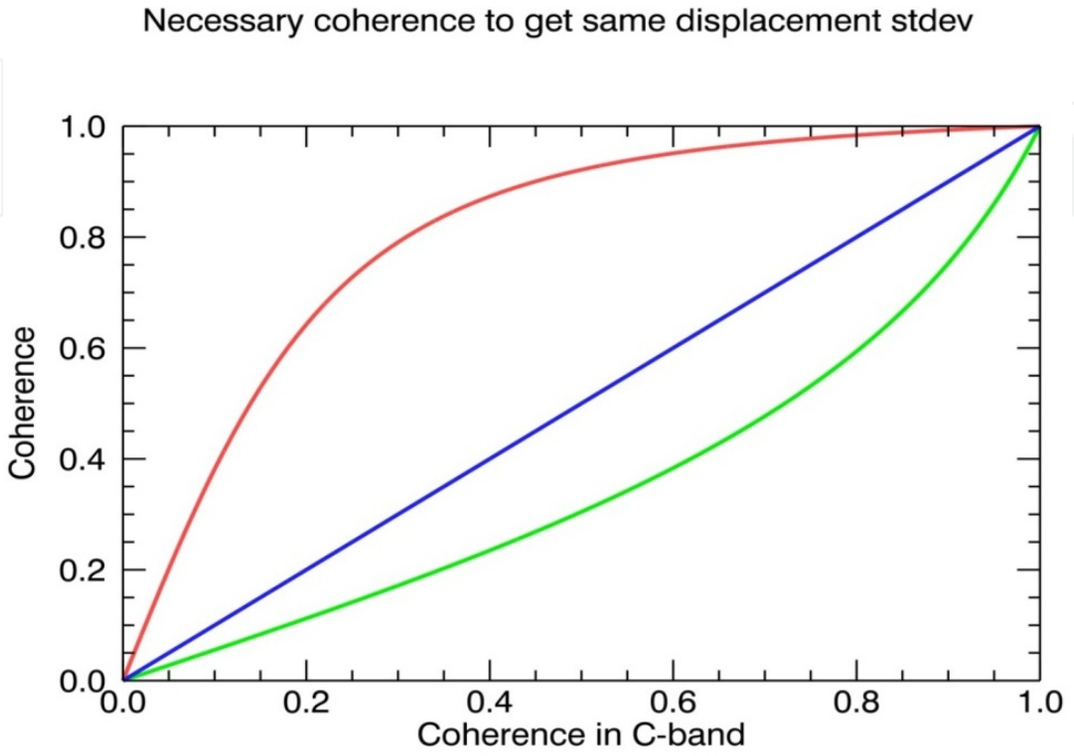


**Figure 2.** Interferometric coherence necessary to obtain the same measurement precision in mm as depending from the different system frequency. Red: L-band; Blue: C-band (reference); Green: X-band.

The amount of temporal decorrelation and hence of phase noise depends itself of the characteristics of the observed areas in relationship with the system wavelength. It is well known that repeat-pass SAR acquisitions are showing complete decorrelation over water bodies, and very high correlation over point targets and man-made features, independently from the system wavelength. On the other hand natural, distributed objects show temporal correlation that depend on the observation frequency: in general the higher the system frequency (and hence the shorter the wavelength), the shorter the penetration of the transmitted signal into vegetation layers, and hence the stronger the effects of temporal decorrelation.

Summarising, it can be expected that lower frequency (e.g. L-band) systems show more extensive coverage over natural areas than systems with higher (e.g. C-and X-band) frequency; on the other hand, where measurements can be obtained with systems with different wavelength on a same area, better precisions can be expected from the systems with shorter wavelength.

One example of these effects is shown in Figure 3, where average displacement rates obtained from stacks of PALSAR-1 (on the left) and of ENVISAT ASAR data (on the right) spanning a period between 2006 and 2010 are presented for a region in Japan between the cities of Tokyo

and Chiba. It is evident here how many black (no value) areas are visible in the ASAR data, while the same regions show reliable measurements obtained with PALSAR data. On the other hand, areas that are covered by both systems show higher variability and hence most likely poorer precision in the PALSAR dataset.

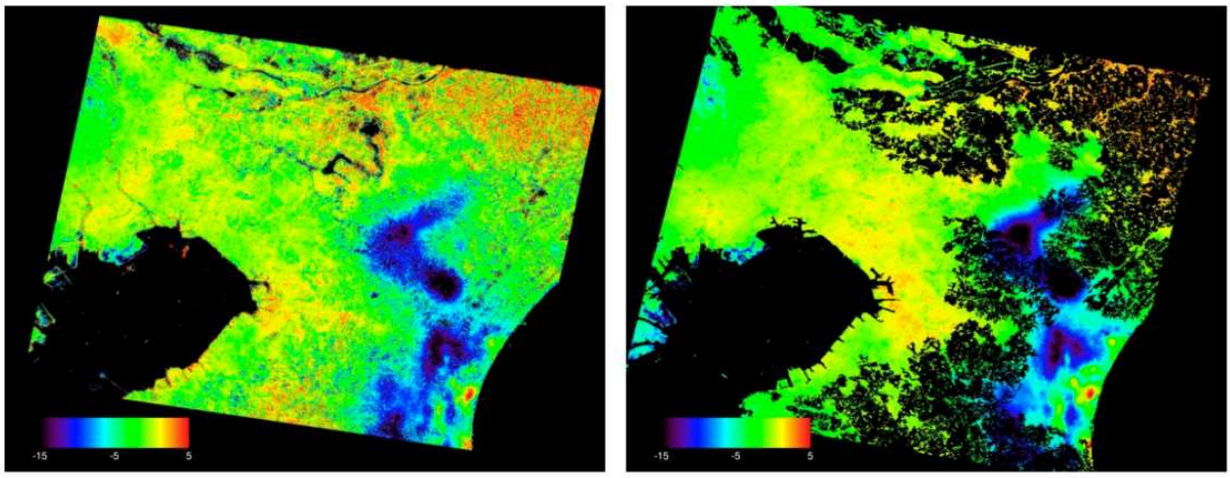


**Figure 3.** Comparison of average displacement rates (color scale between-15 mm/year in blue and+5mm/year in red) as derived with SBAS from ALOS PALSAR (left) and ENVISAT ASAR (right) data over the Tokyo – Chiba area (Japan).

It shall be noticed that models have been proposed to help quantifying the expected temporal evolution of the interferometric coherence (as for example in [7]); a limitation of these approaches is that they focus more on a general, statistical point of view, without considering phenomenological aspects like spatial variability of the land cover [8] and seasonal and long-term effects [9] [10]. It has been seen how these last aspects have finally effects that can be foreseen only in a qualitative way, but of such importance on the decorrelation to significantly decrease the applicability of the theoretical models.

One example is the temporal coherence obtained with very-high resolution X-band systems like TerraSAR-X and COSMO-Skymed: the values measured from real data are often surprisingly higher than that forecasted by models. This is not actually due to the system frequency but more by their very-high spatial resolution: if the backscatter signal measured by coarser resolution system (e.g. ~25m for ERS-1/2 and ASAR) is a mixture of returns from different land cover types (vegetation, bare soil, rocks etc.), and the contribution of stable scatterers is often hidden by the other components, the very-high resolution data (e.g. ~3m for TerraSAR-X and COSMO-Skymed) have higher likelihood of keeping the different contributions separate in different pixels, hence stable scatterers can be better identified as highly coherent pixels.

Some phenomenology may also have an effect on the temporal variability of decorrelation: on one hand, it is commonly assumed that interferometric coherence decreases with time; on the other hand, long time, such as winter-winter interferograms (hence computed for seasons where vegetation changes are typically negligible), often show coherence higher than short-time interferograms computed within periods of strong vegetation changes (e.g. spring).

http://dx.doi.org/10.5772/58225

### 3.1. Validation

Two main approaches may be identified for the validation of the measurements obtained with interferometric stacking techniques: absolute methods for evaluating the accuracy of the measures based on external, reference measurements obtained for example with GNSS, levelling or other systems (e.g. [11] [12] [13]), and more relative methods, evaluating the precision of the SAR-based measurements by comparing results obtained from different sensors (e.g. [13]) and / or different processing approaches (e.g. PS and SBAS).

This Section presents results obtained with both approaches about the validation of interefrometric stacking PS and SBAS measurements from ASAR and PALSAR data over the area in Japan shown in Figure 3, to highlight the different issues relative to validation and typical results in terms of accuracy and precision obtainable with these techniques.

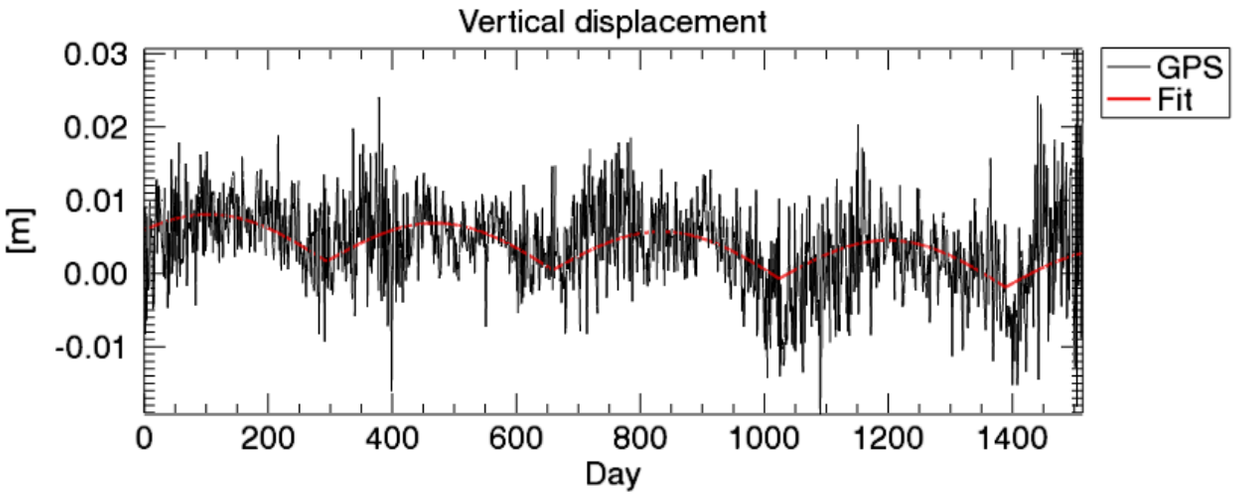


**Figure 4.** Vertical displacement of one of the permanent GPS stations of the GEONET network. Black: original GPS measure; red: fitted values. Data courtesy of GSI.

Permanent GPS station measurements from the GSI GEONET nation-wide network [14] have been exploited to perform an absolute validation of the SBAS data. A first investigation of the GPS data highlighted two main effects, easily detectable from Figure 4: GPS data have themselves a certain dispersion, as expected, and systematic trends (most likely due to uncompensated tidal effects [15] [16]) are present, in form of yearly periodical cycles. A straightforward date-by-date difference between the SAR and GPS (projected along the Line Of Sight direction) measurements is therefore not feasible, and a different strategy shall be adopted. A simple model, composed by a linear displacement combined with a half-cycle sinusoidal oscillation with yearly period, has been selected to describe the GEONET data, and the corresponding parameters have been estimated independently for each of the stations present in the area of study.

Finally, the station-by-station difference between the GENOET fitted linear displacement (re-projected along LOS) and the SBAS average linear displacement has been computed, as shown in Figure 5.

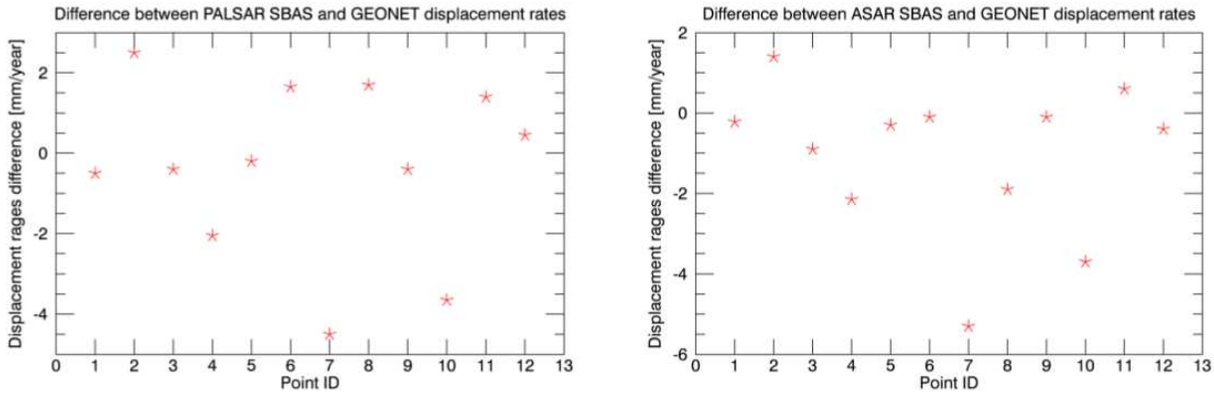


**Figure 5.** Difference between GPS and SBAS PALSAR (on the left) or ASAR (on the right) linear displacement rates.

A summary of the statistics of the differences between the average displacement rates as measured from SAR and GPS is shown in Table 2, confirming the very high accuracy that can be obtained with the interferometric stacking techniques.

| | GPS - PALSAR | GPS - ASAR |
|---|---|---|
| Mean difference [mm/year] | -0.28 | -1.1 |
| Difference Standard Deviation [mm/year] | 1.9 | 1.8 |

**Table 2.** Difference between GPS and SBAS average displacement rates.

The validation has then been continued by comparing the results obtained from SAR data only, by exploiting independent processing applied either to different input time series, derived from different sensors, or to the same time series but exploiting different (PS and SBAS) approaches.

Figure 6 shows the difference between the average displacement rates presented in Figure 3, showing in general a very good agreement between the measures derived from L-band and C-Band data.

Figure 7 shows the differences between average displacement rates obtained with the same sensors but with different (PS and SBAS) methodologies. It can be seen here how in both cases the two approaches provide very similar results but, as expected, the PALSAR (L-band) data show higher variability, due to the longer wavelength and hence smaller sensitivity to displacements.

The statistics summarising the results shown in these figures are presented in Table 3, confirming the comments made on the single plots.

As a final, qualitative cross-validation, displacement time series are shown in Figure 8 for a same pixel as obtained from different data and with different algorithms. Here again, as for the average displacement rates, it can be seen how longer wavelength data provide higher

http://dx.doi.org/10.5772/58225

variability of the measures; on the other hand, SBAS time series show consistently less dispersions when compared with PS time series, mainly due to the filtering performed during the SBAS interferometric processing.

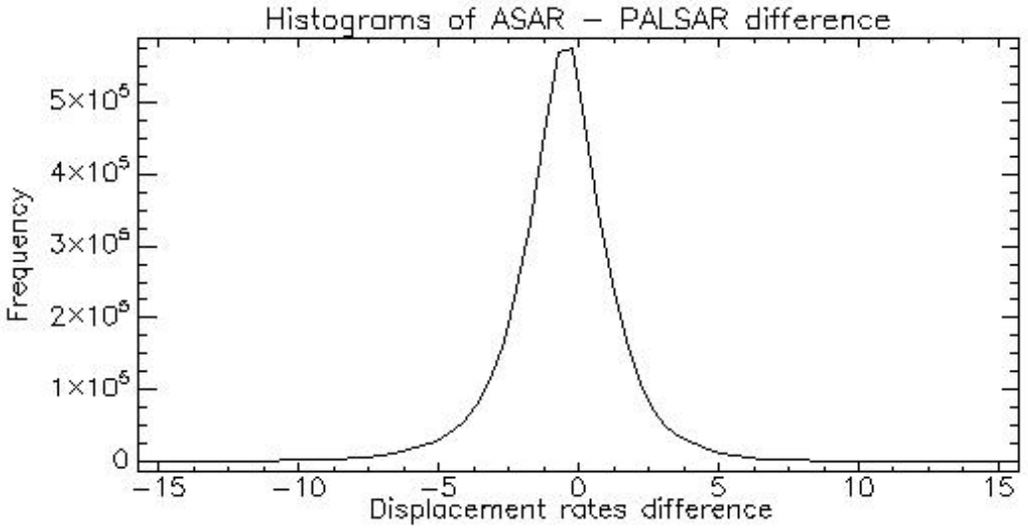


**Figure 6.** Difference between SBAS PALSAR and ASAR linear displacement rates.

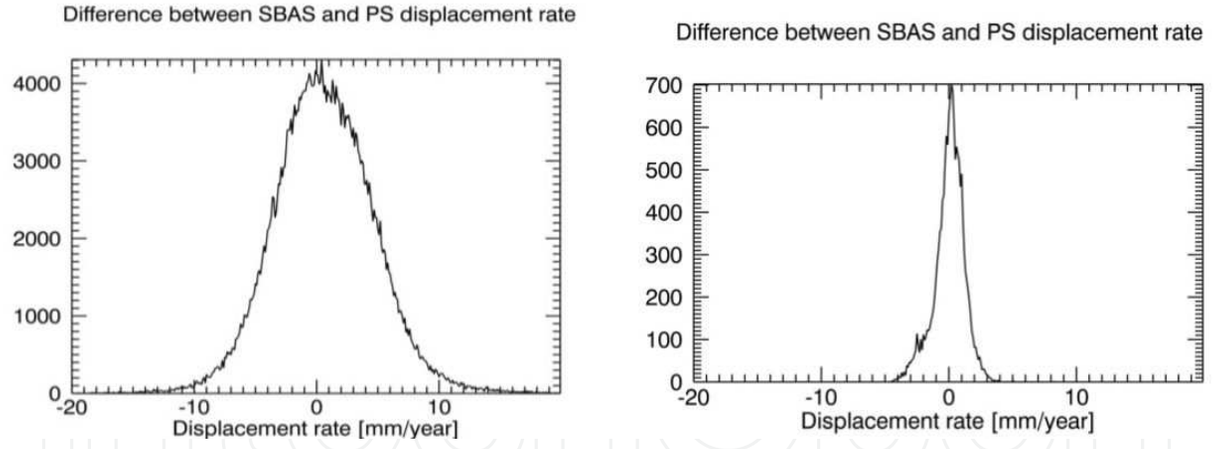


**Figure 7.** Difference between SBAS and PS displacement rates as derived from PALSAR (on the left) and ASAR (on the right) data.

| | SBAS ASAR -PALSAR | PALSAR SBAS – PS | ASAR SBAS – PS |
|---|---|---|---|
| Mean difference [mm/year] | -0.33 | 0.7 | 0.1 |
| Difference Standard Deviation [mm/year] | 2.1 | 4.1 | 1.2 |

**Table 3.** Difference between average displacement rates obtained from PS and SBAS from ASAR and PALSAR data.

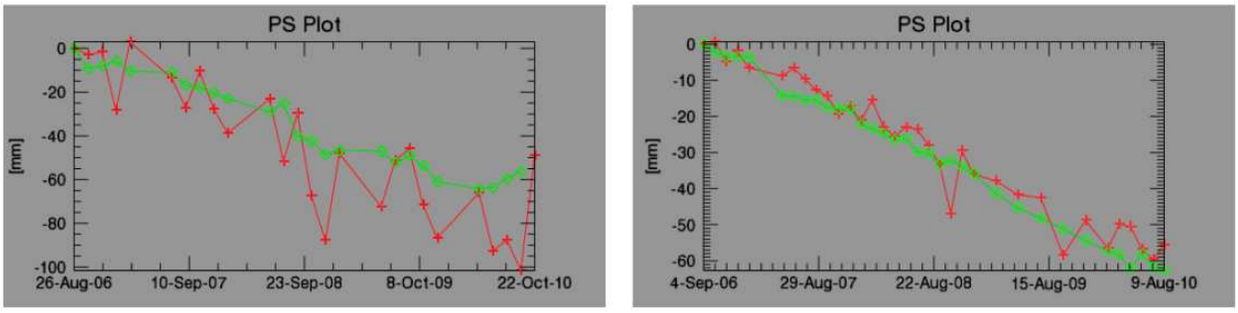


**Figure 8.** Comparison of displacement time series as derived from ALOS PALSAR (on the left) and ENVISAT ASAR (on the right) data exploiting the SBAS (green diamonds) and PS (red crosses) techniques.

### 3.2. Application examples

Some examples are shown in this Section to discuss the applicability of the major interferometric stacking techniques in areas characterised by different land cover, different types of displacements and in view of various land applications.

Figure 9 shows first the average displacement rates as obtained from very-high resolution TerraSAR-X data through PS processing for an area of the city of Budapest, where a new Metro line was under construction, and generally a high PS density could be obtained. A trace of the line is drawn over the area, and the average displacement rate shows in general measurable displacements of subsidence around this trace. The red square indicates the area where the new Metro station of Szent Gellért had been built: a poor PS density is unfortunately achievable here. The middle image in this Figure shows a close-up of the average displacement rate as obtained for the same small area through SBAS processing; the spatial density of measures is much higher in this case, in particular in the area of more severe subsidence.

As the time series shows in the lower image, the displacement is strongly non-linear in this area, characterized in particular by a sudden descent, in the order of magnitude of half of the system wavelength, in a period of about 3 months. This kind of step cannot be resolved well by the PS approach, that tends to fit a linear velocity to the other parts of the time series, but obtaining large residuals, and hence low temporal coherence, discarding the pixels as no PSs. The SBAS approach is on the other hand, also thanks to the very-high resolution of the imagery, capable of obtaining reliable results, and well reconstructing the temporal behaviours of the displacement, that shows good spatial correlation.

Figure 10 shows the historical evolution of the landfills close to Urayasu (Japan). The average displacement rate in the period 2006 – 2010 in the same region, as obtained through PS and SBAS processing of ASAR and PALSAR data is shown in Figure 11. It shall be noticed that these data are a portion of the data shown in Figure 3.

The coverage obtained with the two methods from different data is in this urban area very similar. As expected, the SBAS data show smoother results, while the spatial resolution obtained in the PS case is better and many spatial details are more accurately preserved; PALSAR data show higher spatial variability, while ASAR data provide higher accuracy.

http://dx.doi.org/10.5772/58225

Nevertheless, all 4 approaches provide very consistent results, able to well delineate for example areas of terrain compaction at the borders of different land-fills. It is furthermore interesting to notice how the areas undergoing large subsidence correspond to those having thick layers of soft soil over stiff basement, as shown in Figure 12.

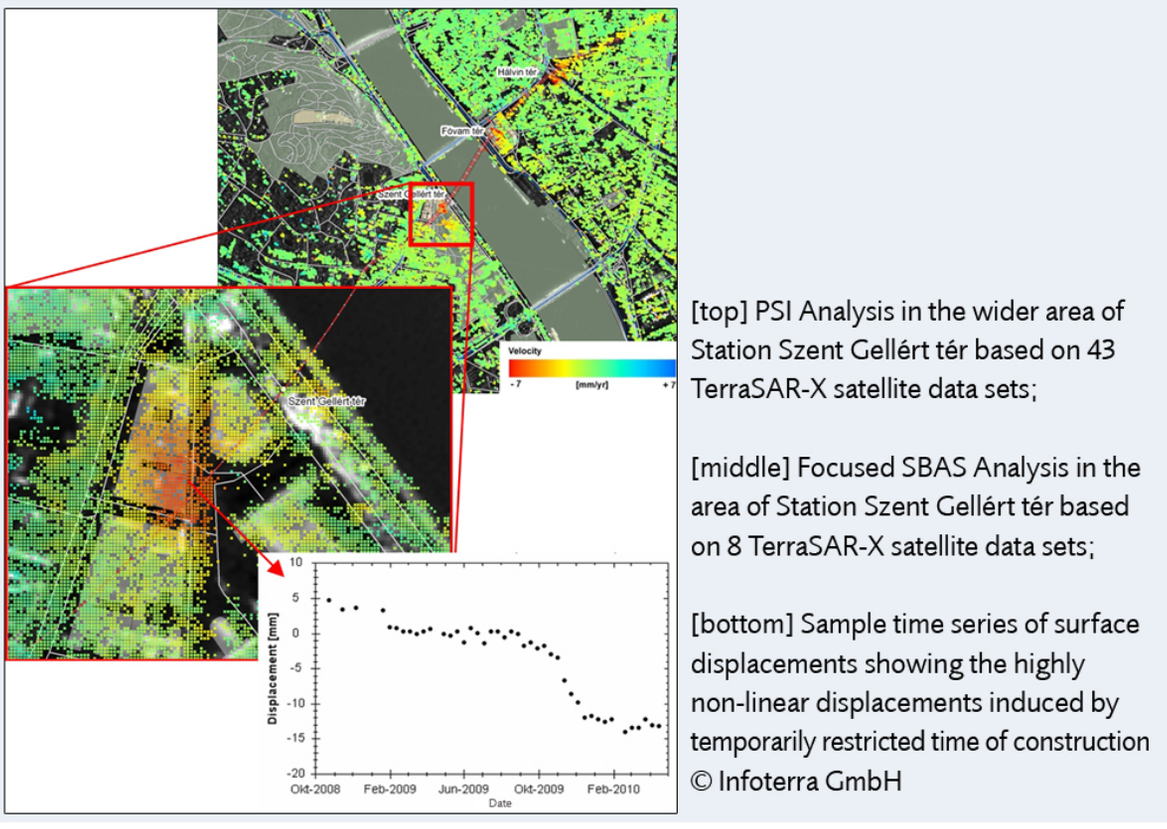


**Figure 9.** Average displacement rate as obtained through PS (above) and SBAS (middle) processing; SBAS displacement time series (below) for an area in Budapest (Hungary). ©Airbus Defence and Space

**Figure 10.** Landfill area around Urayasu (Japan) in years 1950, 1975, 1980 from left to right [17].

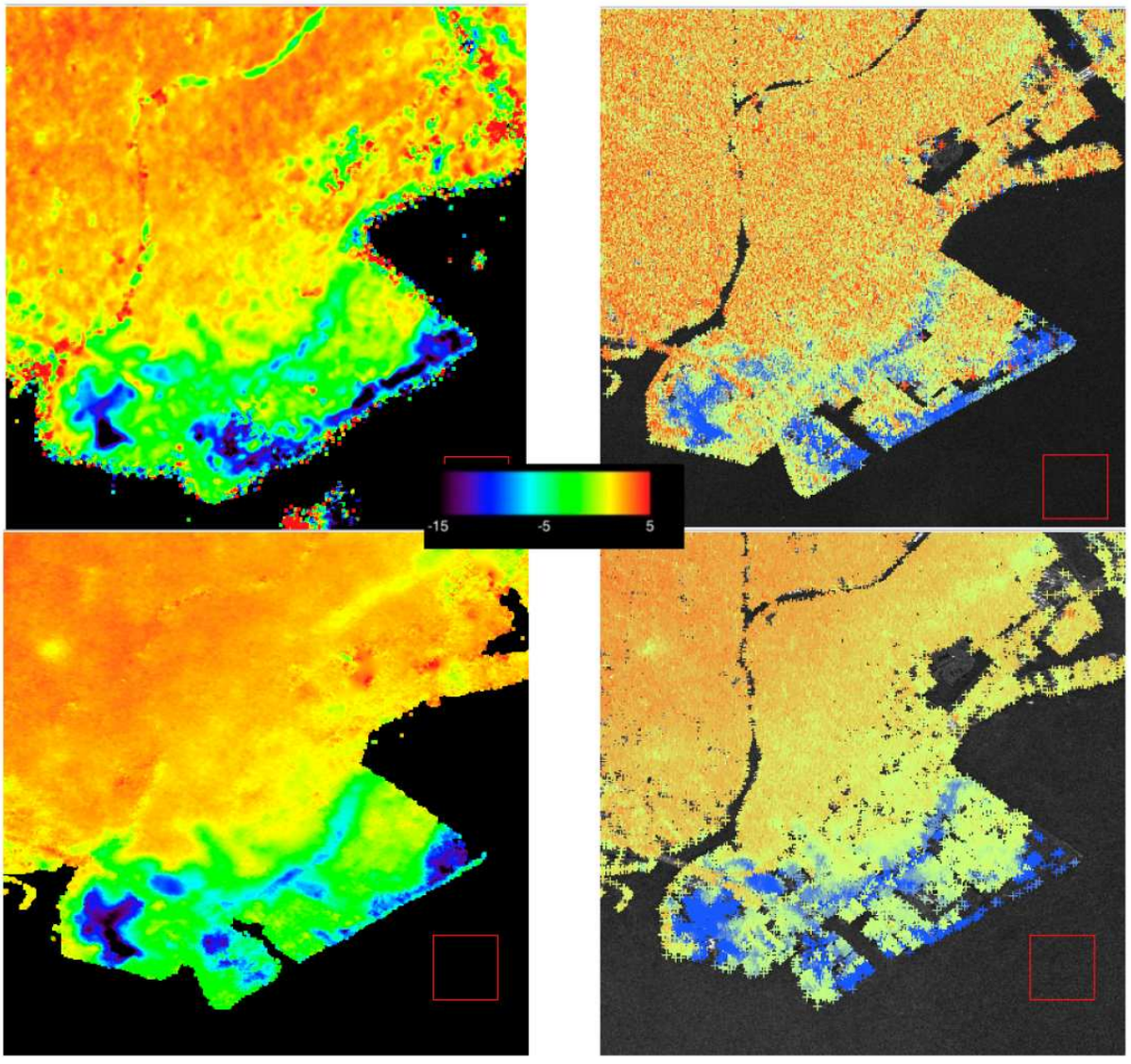


**Figure 11.** Average displacement rate in the 2006-2010 period in the area of Urayasu, as obtained from PALSAR (above) and ASAR (below) data through SBAS (on the left) and PS (on the right) processing.

http://dx.doi.org/10.5772/58225

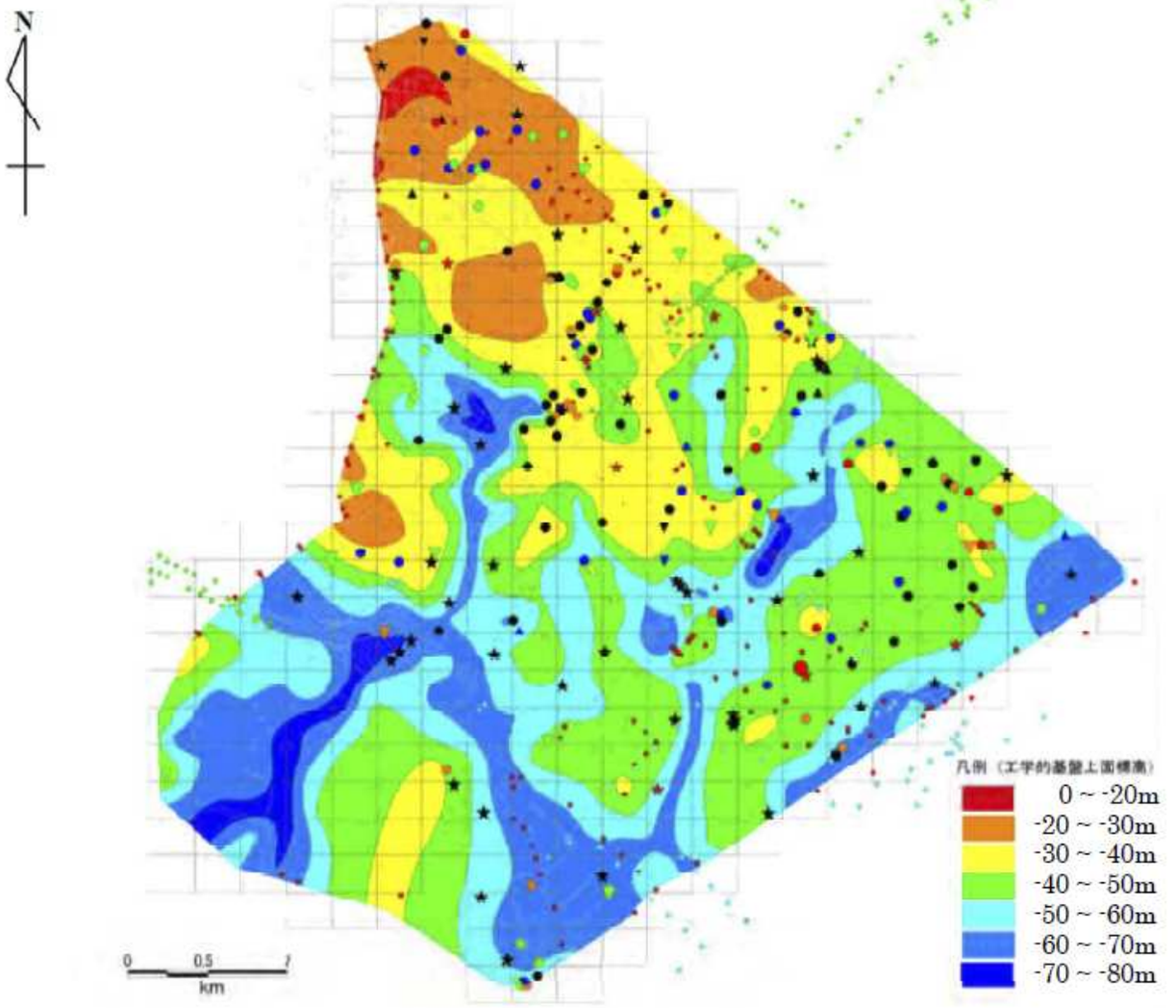


**Figure 12.** Depth of the upper surface of the solid geological stratum (Pleistocene sand stratum with the standard penetration test N value > 50) in Urayasu city [18].

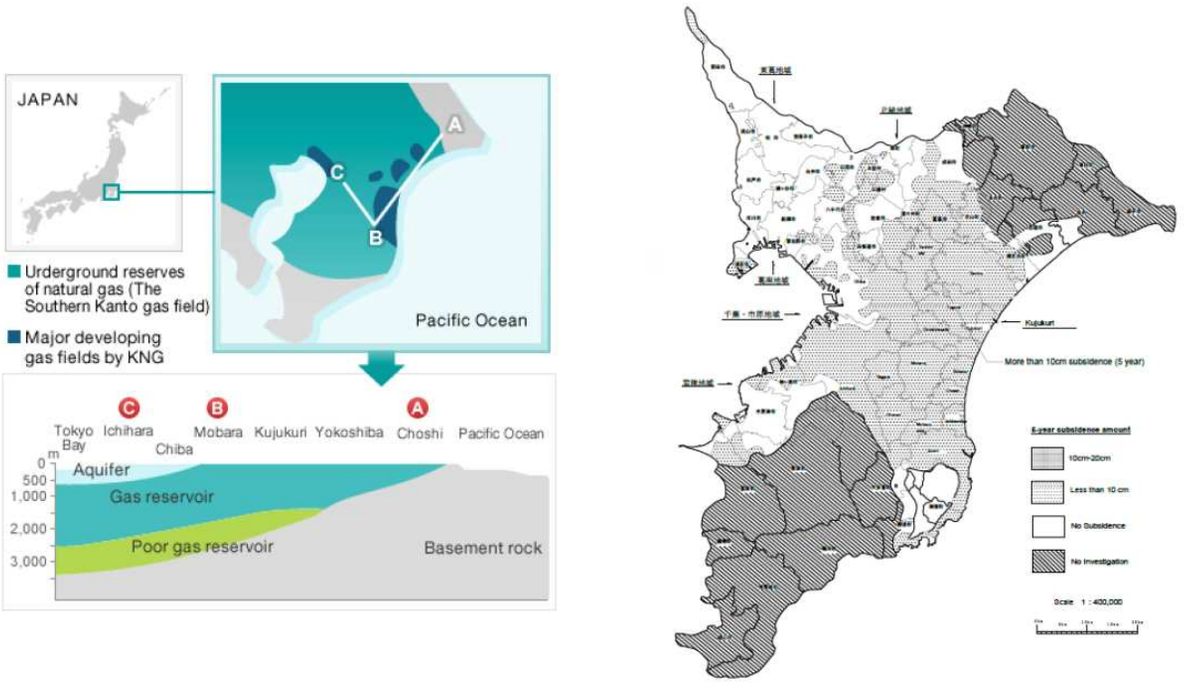


**Figure 13.** Southern Kanto gas field, Kanto Natural Gas Development Co Ltd. [19] (on the left); known 5-years displacement in the region of Togane, eastern part of the same area [20] (on the right).

The whole region of Figure 3 is located over the Southern Kanto gas field [19], shown in Figure 13. Various phenomena of subsidence are known in this region [20], in particular on its eastern side, as shown in the same Figure. This information provide an additional clear indication, although in this case from a qualitative point of view since too coarse respect to the SAR data, about the reliability of the results obtained with the SBAS approach, both in terms of order of magnitude of the average displacement rate and of its spatial distribution.

A closer look at the region on the east coast is shown in Figure 14 as obtained through PS and SBAS processing of ASAR and PALSAR data. An area of uplift is present here, resulting from strong water injection as compensation of the gas extraction. Appropriate coverage can be obtained here only with the SBAS approach, or exploiting PALSAR data and PS processing, while ASAR data and PS processing are providing no reliable results and loosing most of the spatial variation of the displacement. As expected, lower frequency data show rougher spatial distribution; nevertheless, the three applicable approaches show very consistent results both in terms of value and spatial distribution of the obtained results.

Finally, Figure 15 shows the average displacement rate obtained from ASAR imagery over the Lisan peninsula, an area in the Dead Sea characterised by diapirism and severe subsidence phenomena related to the lake level lowering (1m/year), with the PS and the SBAS approaches.

Although the area is very dry and stable from the radar backscattering point of view, the complex land cover and the very complex displacement regimes result in a significantly different spatial coverage obtained with the PS and SBAS methods, making only the second one suitable for reliable investigations in such cases.

http://dx.doi.org/10.5772/58225

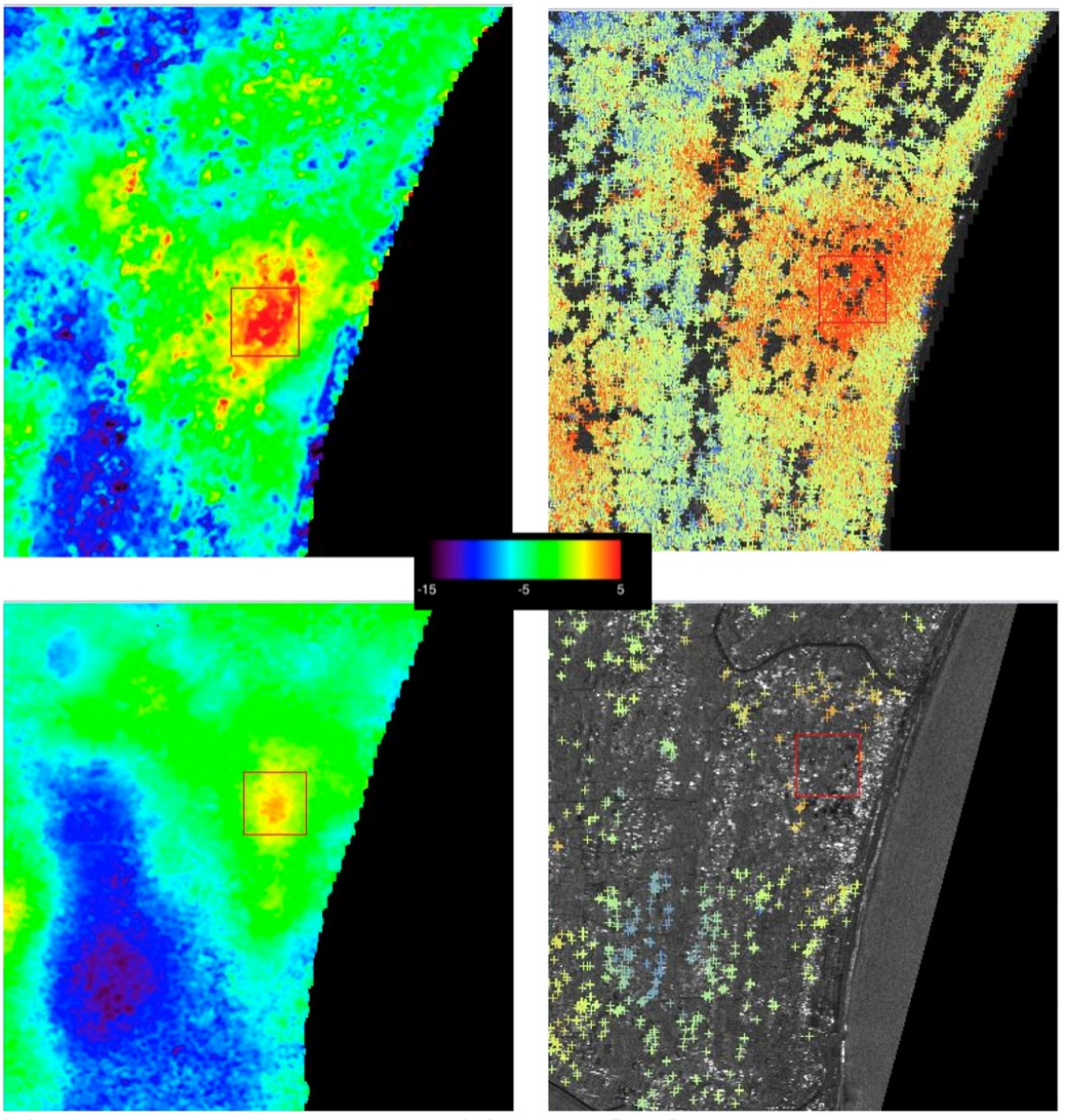


**Figure 14.** Average displacement rate in the 2006-2010 period in the area of Chosei (Japan) obtained from PALSAR (above) and ASAR (below) data through SBAS (on the left) and PS (on the right) processing.

More in-depth analysis of SBAS results for ground deformation monitoring over the Dead Sea region are presented in the Chapter *„Dikes stability monitoring versus sinkholes and subsidence, Dead Sea region, Jordan*" of this book.

## 4. Analysis of time series non-linearity

The exploration performed in the previous Section concerning the exploitability of Interferometric Stacking techniques mainly focused on the analysis of the average displacement rate as measured on a stack of SAR imagery. On the other hand, as already mentioned in the previous

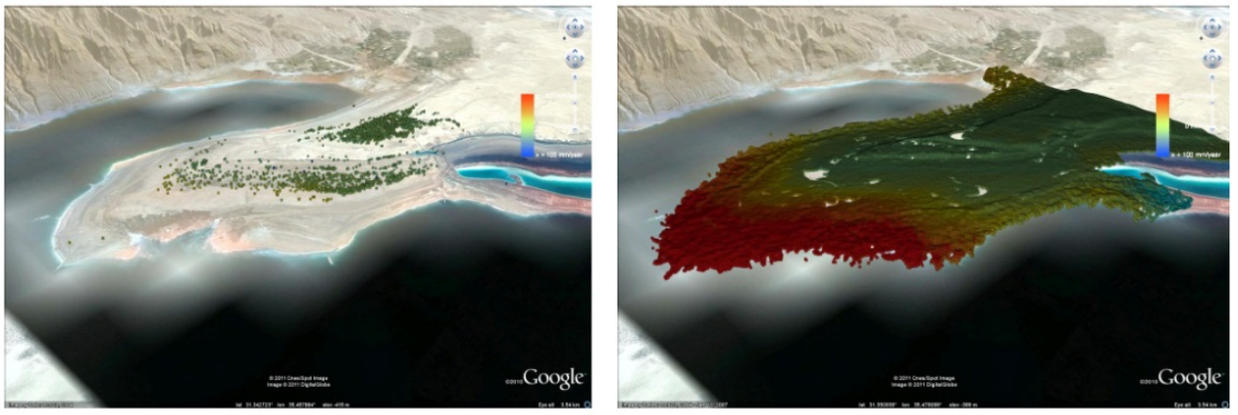

**Figure 15.** Comparison of average displacement rates in the period 2003 – 2010 as derived with PS (left) and SBAS (right) processing from ENVISAT ASAR data over the Lisan peninsula, Dead Sea, Jordan.

Sections, the information that can in principle be extracted from such input data is far more, not only limited to a simple average value, but potentially describing the full temporal evolution of phenomena that vary with the time.

One evident advantage of exploiting the average displacement rate is that it can be easily displayed, and regions showing different average behaviours can be easily identified with a simple visual analysis. These observations start to show their limitation as soon as more complex, non-linear behaviours are to be expected (as natural) in a certain region, and different parameters shall be sought to provide a synthetic way to visualise and identify areas with similar, non-linear characteristics.

Figure 16 in the upper left part shows an excerpts of a South-Eastern region of Figure 3 right, for which the average displacement rate is displayed, as estimated through the SBAS algorithm. As previously described, the SBAS algorithm obtains this information through a Lest Mean Square fit / inversion, whose statistical significance is often estimated by measuring the corresponding $\chi^2$ value. When a simple linear model is assumed during the SBAS fit / inversion for this area, the corresponding $\chi^2$ resembles what is shown in Figure 16 upper right; two regions can be easily identified in this image, showing systematically high values of $\chi^2$, hence good candidates for a further investigation, focused on the identification of non-linear displacement behaviours. Figure 16 shows in the lower row temporal plots for the two regions highlighted in the $\chi^2$ image; the plot on the left in particular shows in red the displacement time series of the point in region 1 showing highest $\chi^2$ values, while in blue (as comparison) the time series of a neighbouring pixel that shows low values of $\chi^2$. The same Figure shows in the lower right part in red the displacement time series of the point in region 2 showing highest $\chi^2$ values, while in blue (as comparison) the time series of the neighbouring pixel that shows largest average displacement rate, as in the upper lower image of the same Figure, but linear variation.

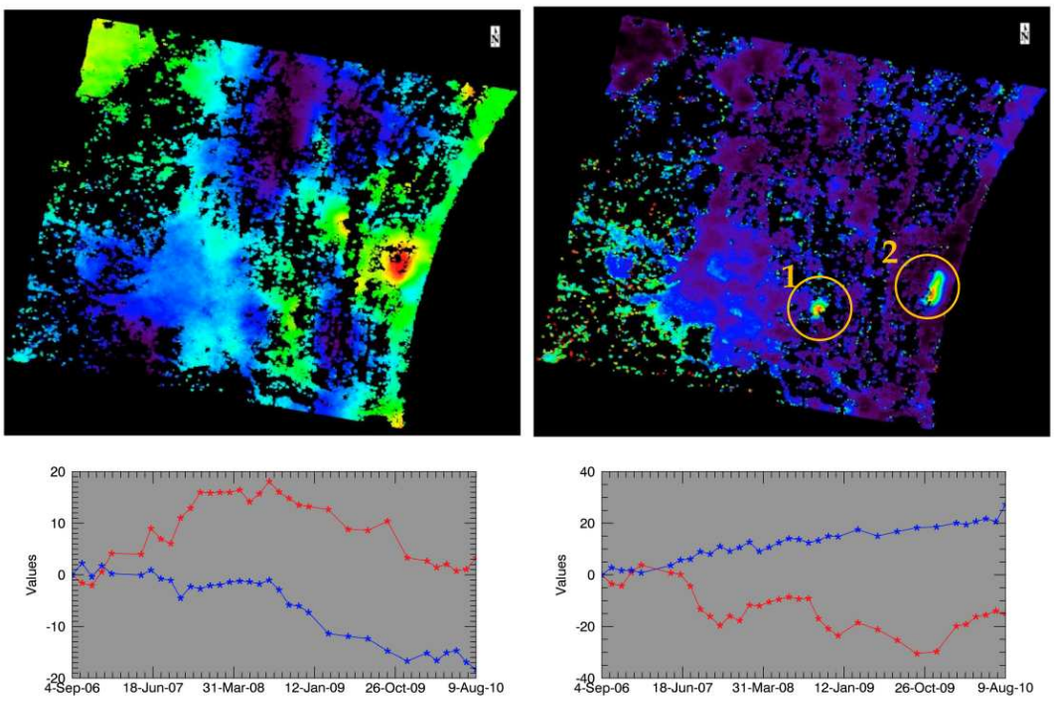


**Figure 16.** ENVISAT ASAR SBAS results over the Togane region (Japan). Left to right and top to bottom: average displacement rate, χ2 from linear model, location time series in [mm] from areas 1 and 2 in the χ2 image.

The plots in this Figure show very clearly two different non-linear behaviours: area 1 is characterised by a parabolic (first increasing an then decreasing) trend, while area 2 is characterised by a periodical trend, with a yearly cycle. As it can easily be seen, these two regions could not at all be identified from the average displacement rate image, while their temporal behaviours significantly deviate from a linear one, that characterizes most neighbouring regions.

The $\chi^2$ value seems hence a good candidate for a simple yet efficient identification of areas showing non-linear but consistent temporal displacement behaviours, as identified by the SBAS processing.

As a further trail, the $\chi^2$ value has been evaluated again after performing a new SBAS processing that considers a 3rd order polynomial model during the inversion steps; the corresponding result is shown in Figure 17. Here it can be easily seen how the $\chi^2$ value is significantly reduced in region 1, that originally showed parabolic trends, hence easily fitted with a third order model; the same cannot be said for region 2, where the periodical trend cannot be easily described by a polynomial function.

Another non-linearity analysis example is presented in Figures 18-24 for a region in Jordan close to Madaba city, where land subsidence relates with water extraction for agricultural practices.

Figure 18 shows the average displacement rate estimated with a liner model and the corresponding $\chi^2$. It is interesting to notice that, although the two measures show large values

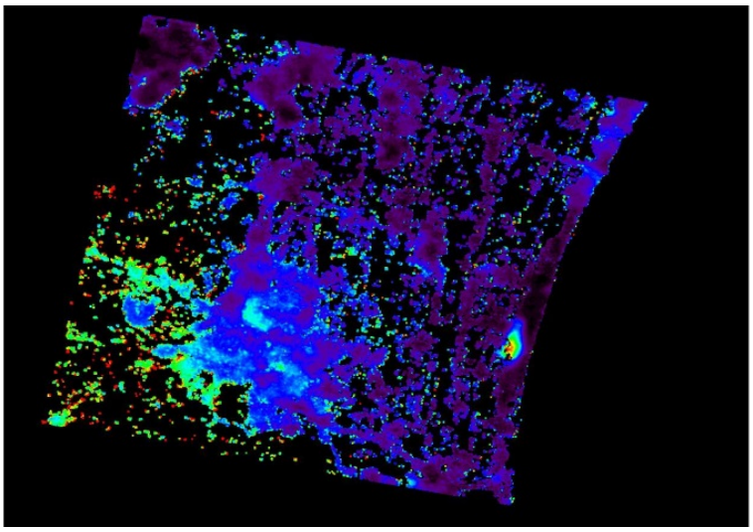

**Figure 17.** ENVISAT ASAR SBAS results over the Togane region (Japan), χ2 from cubic model.

generally in the same geographic area, their spatial distribution is quite different; most of large displacements are characterised by strongly non-linear motions, but not all and not in the same way, hence the average displacement rate layer is not showing all the information.

Figure 19 is presenting results obtained on the same area by exploiting a cubic deformation model. As to be expected, the accuracy of the fit of the SAR time series increased (and hence the $\chi^2$ values decreased), and most of the displacements can be statistically well described by a 3rd order polynomial.

Figure 20 shows the difference between the $\chi^2$ values as resulting from the linear and respectively cubic polynomial fit. As expected, most of the image shows no significant change, i.e. the linear model is good enough to describe the displacement behaviour. On the other hand, a few areas show significant decrease of the $\chi^2$ values when increasing the model complexity. Some of them have been highlighted in the same Figure, and their displacement time series is shown in Figure 21, together with that of an area with large displacement rate but already low $\chi^2$ values, highlighted in Figure 18.

Here it can be seen how the non-linear displacement in area 1 is characterised by a first almost linear regime, followed by a significant acceleration and finally a possible little deceleration. Areas 2 and 3 show similar behaviours, where the initial linear trend is almost constant (no displacement) and the final deceleration is possibly less pronounced. All three cases seems nevertheless well suitable for a cubic polynomial representation; a further information that could be of interest for the exploitation is the date of change between the linear (or constant) and the accelerated regime.

Area 4 shows a quite clear quadratic behaviour, that could have equally well fitted with a second order model.

http://dx.doi.org/10.5772/58225

Area 5 presents, on the contrary, a simple linear regime that, even if the average displacement rate is quite large, could be well fitted with a first order model, showing no significant improvement (reduction) in the $\chi^2$ values when increasing the model complexity.

It might be of interest at this point to comment the average acceleration and acceleration variation images shown in Figure 22, as estimated with the third order model.

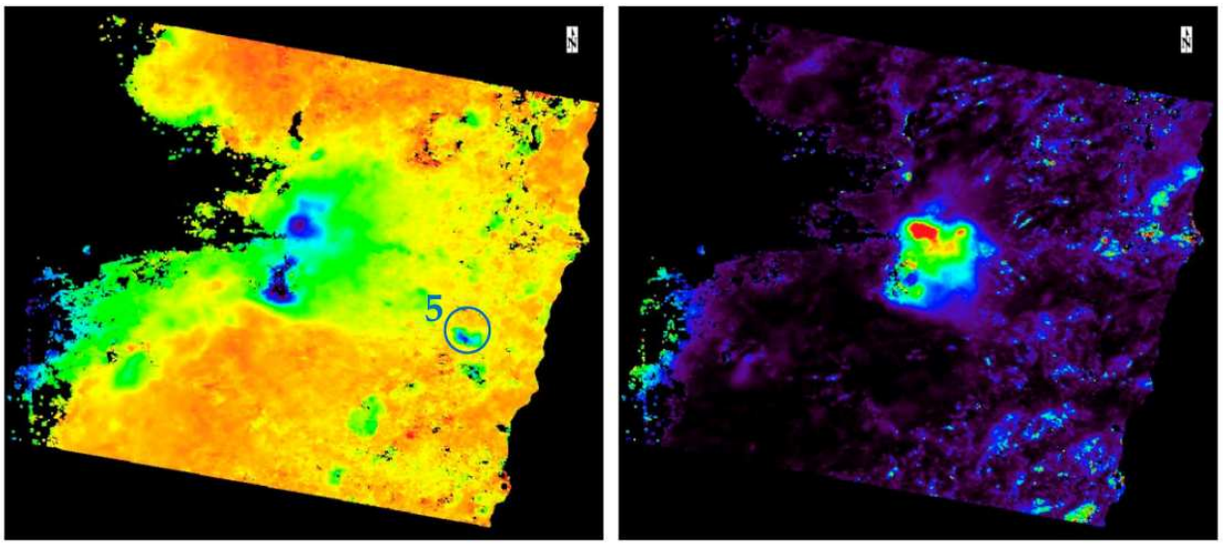


**Figure 18.** ENVISAT ASAR SBAS results over the Madaba region (Jordan). Average displacement rate from linear model (on the left) and corresponding χ2 (on the right).

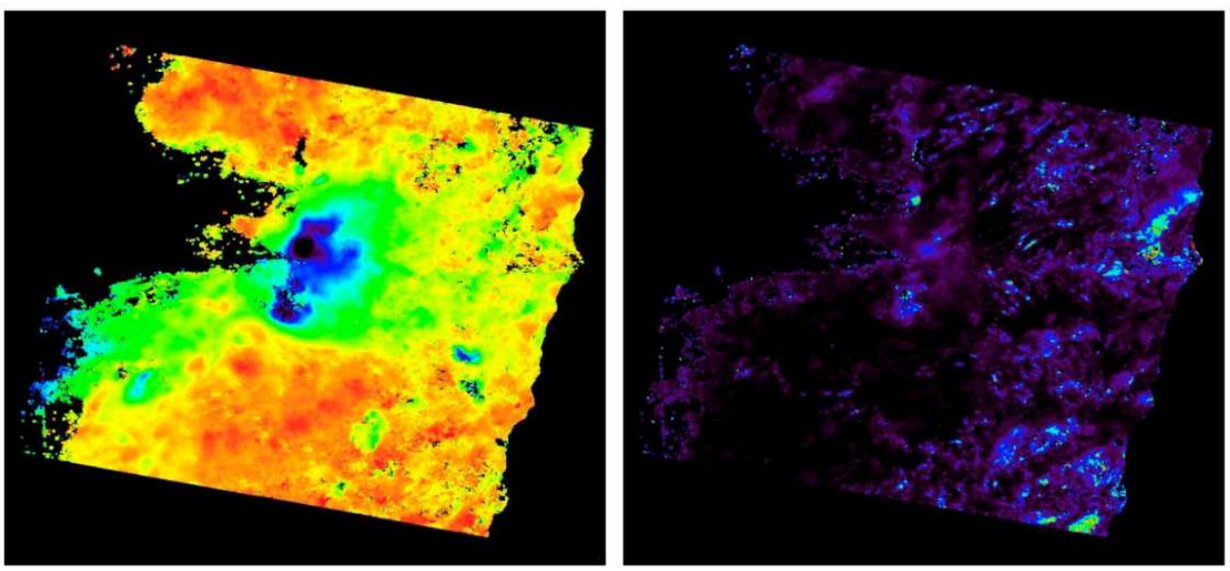

**Figure 19.** ENVISAT ASAR SBAS results over the Madaba region (Jordan). Average displacement rate from cubic model (left) and corresponding χ2 (right).

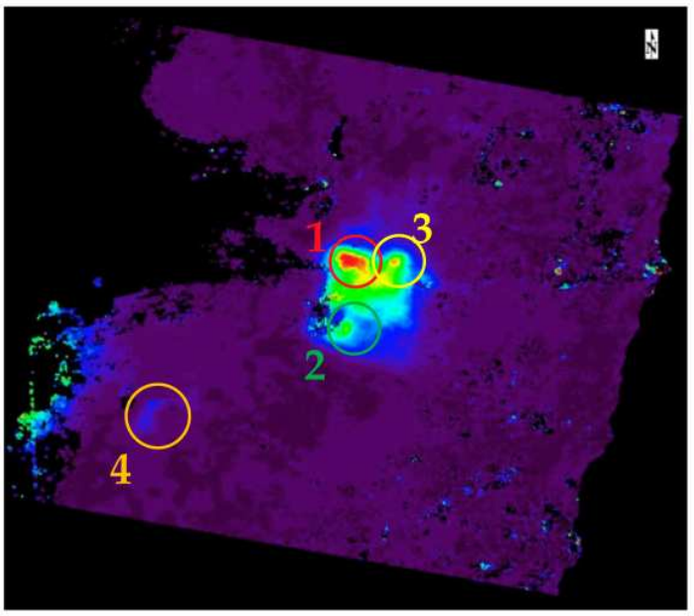


**Figure 20.** ENVISAT ASAR SBAS results over the Madaba region (Jordan). Difference of χ2 between linear and cubic model.

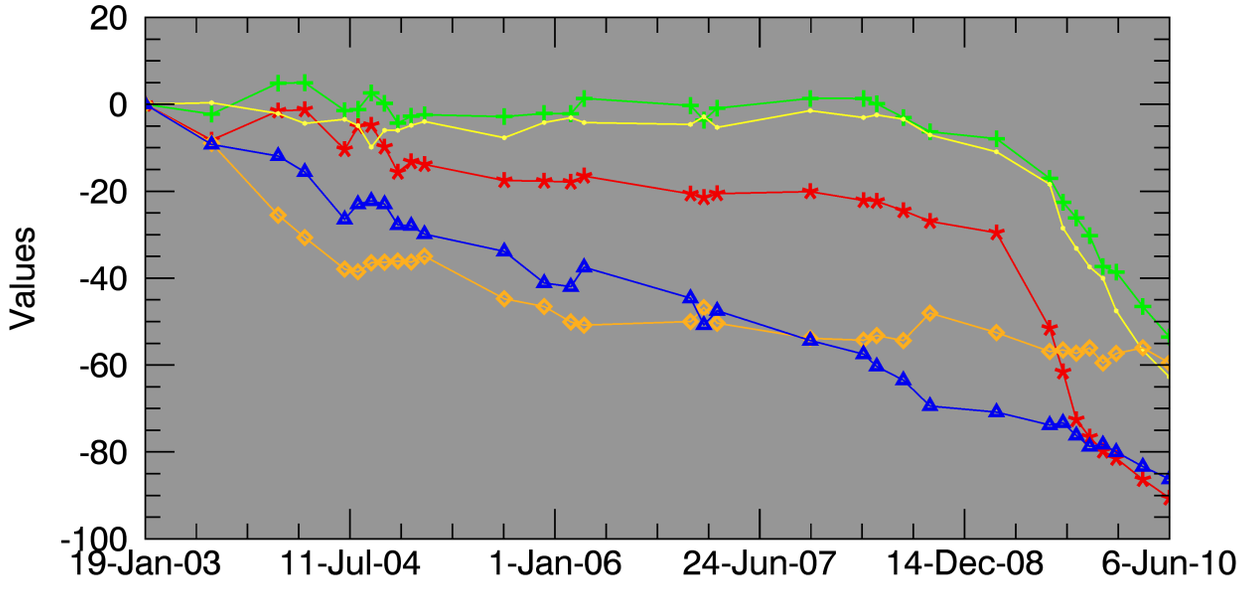


**Figure 21.** Displacement time series in [mm] from areas 1 to 5 of Figure 20 and Figure 18.

The average acceleration provides a measure of the main curvature of the time series: a big part of the area shows very small curvature (green – yellow areas, hence characterised by mostly linear displacements, as for curve 5); areas in red correspond to positive curvatures, with mainly a decrease of the displacement rate with the time, as in curve 4 of Figure 20-21, while blue areas show negative curvature, hence corresponding to an increase of the displacement rate (in absolute value), as in curves 1 to 3 in the same Figures.

http://dx.doi.org/10.5772/58225

It shall be noticed again how these images have again a different although overall similar spatial distribution with respect to the average displacement rate one, showing the amount of additional information on the discrimination of different displacement regimes that they can bring.

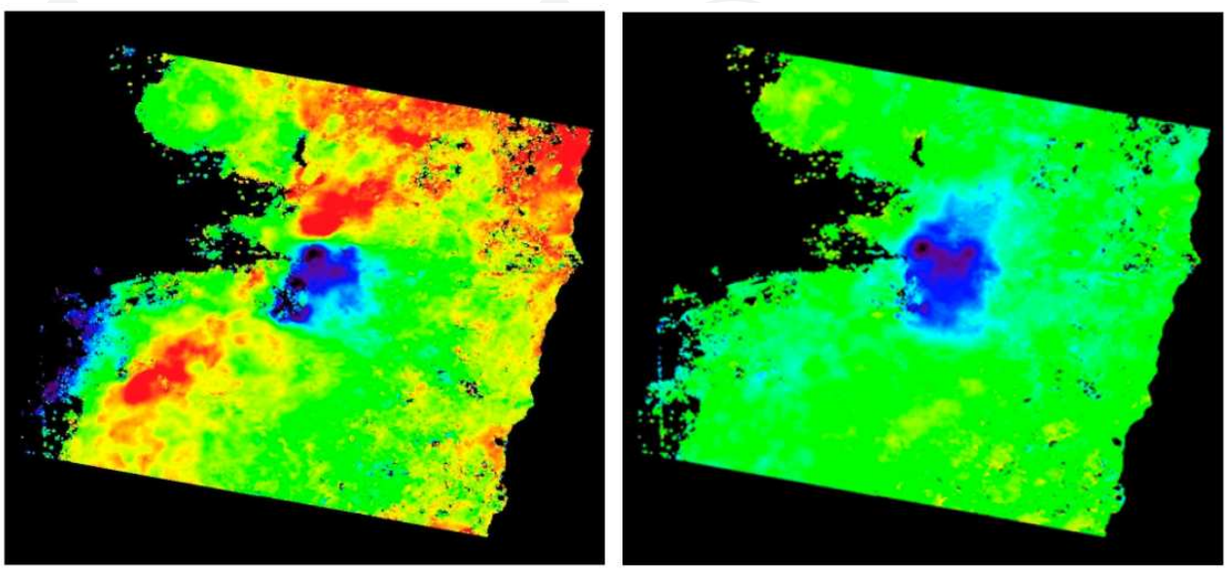

**Figure 22.** ENVISAT ASAR SBAS results over the Madaba region (Jordan). Average displacement acceleration from cubic model (left) and corresponding acceleration variation (right).

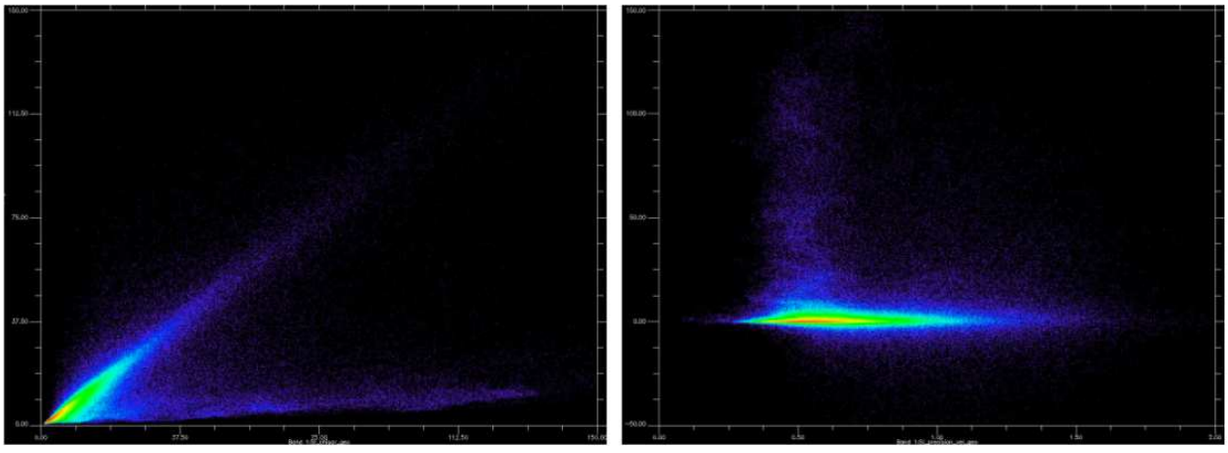

**Figure 23.** ENVISAT ASAR SBAS scatter plots over the Madaba region (Jordan). On the left: χ2 from linear model (x axes) against χ2 from cubic model (y axes). On the right: scatter plots of expected displacement rate precision (x axes) against χ2 decrease from linear to cubic model (y axes).

Figure 23 presents two scatter plots for the same case, where the $\chi^2$ values obtained with the two model types are plotted together (on the left), and their difference is plotted against the value of expected displacement accuracy, as estimated from the original pixels coherence.

The first plot shows, as expected, mainly two groups of pixels, one for which the increase of model order is not making a real difference (mostly linear motions, and some non-linear non-polynomial motions, or noise), and the other for which a higher order model is more appropriate. Mainly no pixel shows significant decrease of the fit accuracy at the increase of the model order.

The scatter plot on the right is on the other hand showing how the increase of the fit accuracy can be obtained only for pixels that, a priori, can be assumed as reliable and for which any analysis or fit of the displacement time series can provide meaningful results.

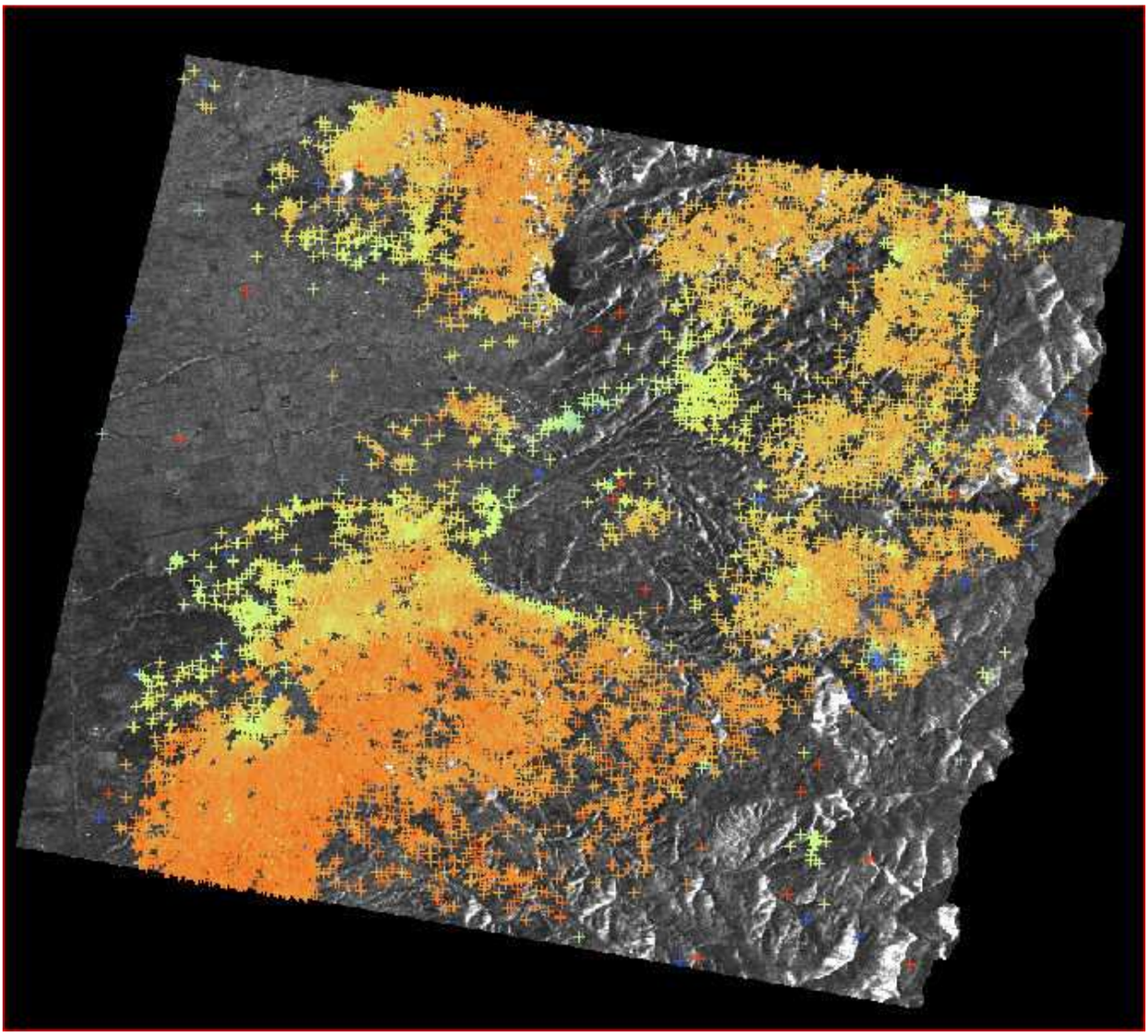

**Figure 24.** ENVISAT ASAR PS results over the Madaba region (Jordan).

Figure 24 shows the results of the PS processing over the same area. It is well visible that reliable results can, with this approach, be obtained only for areas characterised by a well linear

displacement behaviours; area showing large $\chi^2$ values in case of linear model do not provide any result when processed with the PS technique.

The following Table summarises the findings obtained in the analysis of the $\chi^2$ layers of the two previous cases and the information about discriminating different temporal behaviours of the displacements.

| | **Small linear $\chi^2$** | **Large linear $\chi^2$** |
|---|---|---|
| Small cubic $\chi^2$ | Linear motion | Non-linear polynomial motion |
| Large cubic $\chi^2$ | Noisy pixel | Non-linear non-polynomial motion (e.g. periodical – seasonal) |

**Table 4.** Discrimination of different displacement temporal regimes based on $\chi^2$ analysis.

## 5. Conclusions and outlook

The previous Sections presented a number of validated examples, showing how interferometric stacking techniques can provide accurate and reliable information concerning ground deformations that can be very valuable for different applications. The PS and SBAS approaches can be considered as complementary, each with specific unique features.

The huge amount of measures, both in terms of spatial and temporal density, that these techniques can provide, when for example compared with other systems like GNSS or levelling, can be on one hand considered as a wealth of information. On the other hand, such detail can often make the interpretation very complex.

As for example discussed in the previous Section, the average displacement rate is often just one of the synthetic descriptors that can be used to represent in a compressed way the complexity of the whole displacement time series. When the displacement regimes are more complex, robust algorithms as the SBAS one shall be exploited, or adaptations of the original PS approach shall be considered that could extend (even if not completely) its applicability toward more non-linear [21] and / or non-continuously coherent displacements [22]. Other indicators and analysis approaches shall also be developed to help the identification and extraction of the different regimes.

Different physical factors start to play a role in the interpretation of the obtained measurements, as soon as their accuracy start to be very high. It is for example well known that the temperature variations start to be clearly recognisable in interferometric stacking measurements, in particular when performed over large metallic structures (bridges, buildings with big metallic components etc.). One example of such an effect is shown in Figure 25 for an area of the city of Beijing as obtained through PS processing of very-high resolution COSMO-Skymed data. Piles of PSs are visible, corresponding to the reflections of the different floors of single buildings. One of them, in the lower left part of the image is showing average displace-

ment rates that well correlate with its height: higher locations have larger thermal expansion, as to be expected for this tall metallic building.

This component cannot be neglected, and should for example be included within the inversion steps by opportunely modifying the corresponding algorithms [23].

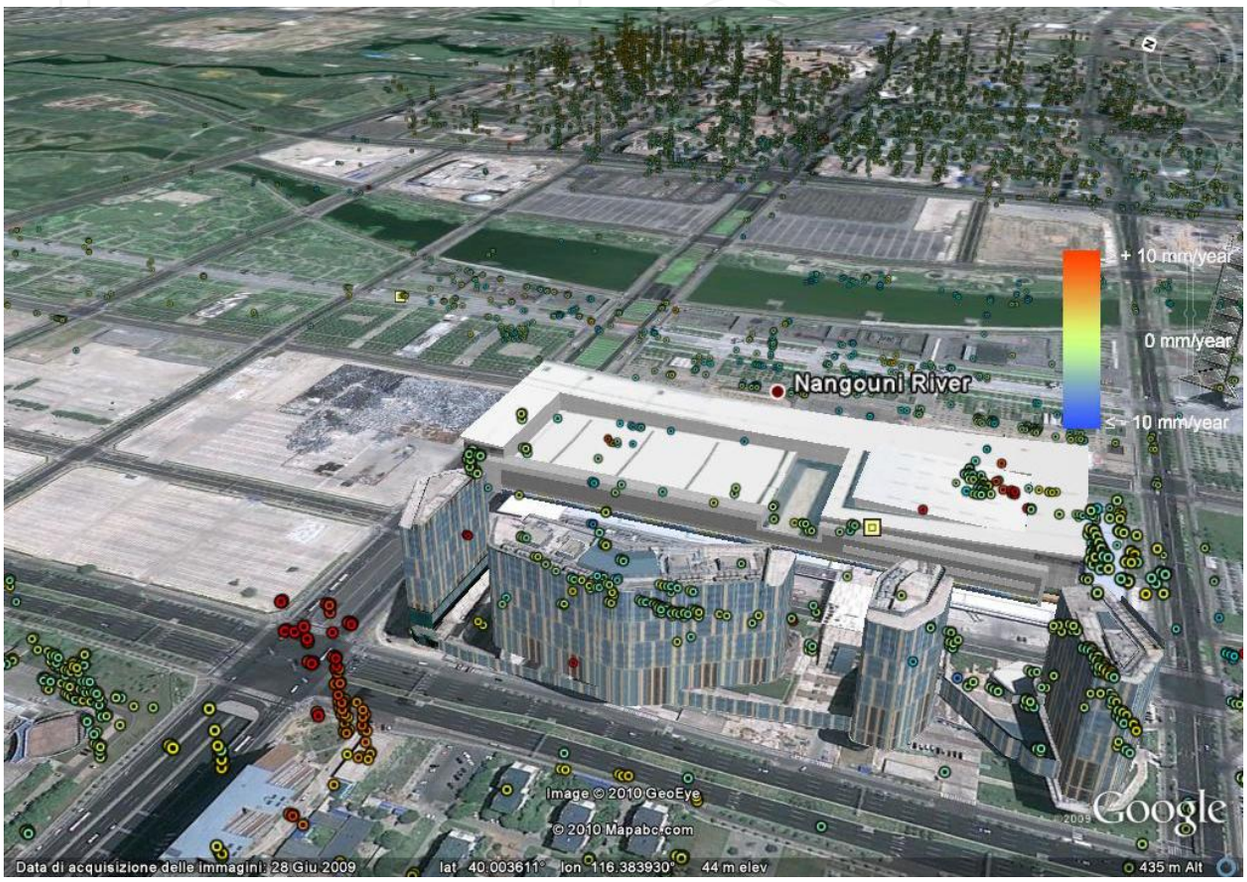


**Figure 25.** Average displacement rate estimated with the PS approach over an area of Beijing from COSMO-Skymed data. Each circle correspond to one identified PS.

As recalled in the previous Sections, all interferometric stacking algorithms include a step of estimation and subtraction of the APS, based on some statistical assumptions on the spatial and temporal distribution of the atmospheric artefacts. These assumptions may be often in contrast with the spatial distribution of the displacement, also considering sometime a similar dependency of the displacement and of the atmosphere parameters with the terrain topography, as for volcanoes and for other specific cases and morphologies. It is hence very interesting to explore alternative approaches, based on additional independent measurements, to estimate and mitigate the impact of atmospheric heterogeneities, as for example as suggested in [24]-[30] with different approaches.

Last but not least, it has been shown how both PS and SBAS provide very interesting and complementary information; approaches that somehow merge the best of the two worlds can hence only considered with big interest [31] [32].

## Author details

Paolo Pasquali[1*], Alessio Cantone[1], Paolo Riccardi[1], Marco Defilippi[1], Fumitaka Ogushi[2], Stefano Gagliano[3] and Masayuki Tamura[4]

*Address all correspondence to: paolo.pasquali@sarmap.ch

1 Sarmap SA, Purasca, Switzerland

2 Exelis Visual Information Solutions K.K., Tokyo, Japan

3 Exelis Visual Information Solutions Italia, Concorezzo, Italy

4 Department of Civil and Earth Resouces Engineering, Kyoto University, Kyoto, Japan

## References

[1] Ferretti, A., Prati, C., & Rocca, F.: "*Permanent scatterers in SAR interferometry*", IEEE Transactions on Geoscience and Remote Sensing, 39, 8-20, 2001.

[2] Berardino, P., Fornaro, G., Lanari, R., & Sansosti, E.: "*A new algorithm for surface deformation monitoring based on small baseline differential SAR interferograms*", IEEE Transactions on Geoscience and Remote Sensing, 40, 2375-2383, 2002.

[3] Gatelli, F., Monti Guarnieri, A., Parizzi, F., Pasquali, P., Prati, C., Rocca, F., "*The wavenumber shift in SAR interferometry*", *Geoscience and Remote Sensing, IEEE Transactions on*, vol.32, no.4, pp.855,865, Jul 1994.

[4] Pepe, A.; Lanari, R., "On the Extension of the Minimum Cost Flow Algorithm for Phase Unwrapping of Multitemporal Differential SAR Interferograms," *Geoscience and Remote Sensing, IEEE Transactions on*, vol.44, no.9, pp.2374,2383, Sept. 2006.

[5] Lanari, R.; Mora, O.; Manunta, M.; Mallorqui, J.J.; Berardino, P.; Sansosti, E., "*A small-baseline approach for investigating deformations on full-resolution differential SAR interferograms*," *Geoscience and Remote Sensing, IEEE Transactions on*, vol.42, no.7, pp.1377,1386, July 2004.

[6] Zebker, H.A.; Villasenor, J., "*Decorrelation in interferometric radar echoes*", *Geoscience and Remote Sensing, IEEE Transactions on*, vol.30, no.5, pp.950,959, Sep 1992.

[7] Rocca, F., "*Modeling Interferogram Stacks*", *Geoscience and Remote Sensing, IEEE Transactions on*, vol.45, no.10, pp.3289,3299, Oct. 2007.

[8] A. Parizzi, X. Y. Cong, and M. Eineder, "*First results from multifrequency interferometry-a comparison of different decorrelation time constants at X, C and L-band*", *Fringe 2009 Workshop Proceedings*, 2009.

[9] Meng Wei; Sandwell, D.T., "Decorrelation of L-Band and C-Band Interferometry Over Vegetated Areas in California," *Geoscience and Remote Sensing, IEEE Transactions on*, vol.48, no.7, pp.2942,2952, July 2010

[10] Parizzi, A., "Speckle statistics and long-term coherent SAR interferograms," *Geoscience and Remote Sensing Symposium (IGARSS), 2012 IEEE International*, vol., no., pp. 5590,5593, 22-27 July 2012.

[11] Persistent Scatterer Interferometry Codes Cross-Comparison And Certification (PSIC4) Project. *http://earth.esa.int/psic4/* (accessed 25 September 2013).

[12] D. Raucoules, B. Bourgine, M. de Michele, G. Le Cozannet, L. Closset, C. Bremmer, H. Veldkamp, D. Tragheim, L. Bateson, M. Crosetto, M. Agudo, M. Engdahl, "*Validation and intercomparison of Persistent Scatterers Interferometry: PSIC4 project results*", Journal of Applied Geophysics, Volume 68, Issue 3, July 2009, Pages 335-347

[13] Ferretti, A.; Savio, G.; Barzaghi, R.; Borghi, A.; Musazzi, S.; Novali, F.; Prati, C.; Rocca, F., "Submillimeter Accuracy of InSAR Time Series: Experimental Validation," *Geoscience and Remote Sensing, IEEE Transactions on*, vol.45, no.5, pp.1142,1153, May 2007.

[14] Miyazaki, S., Y. Hatanaka, T. Sagiya and T. Tada: "*The Nationwide GPS Array as an Earth Observation System*", Bull. Geographical Survey Institute, 44, 11-22, 1998.

[15] Hatanaka, Y., A. Sengoku, T. Sato, J.M. Johnson, C. Rocken and C. Meertens: „*Detection of Tidal Loading Signals from GPS Permanent Array of GSI Japan*", J. Geod. Soc. Japan, 47, 187-192, 2001.

[16] Hatanaka, Yuki, Toyohisa Iizuka, Masanori Sawada, Atsushi Yamagiwa, Yukie Kikuta, James M. Johnson, and Christian Rocken, "*Improvement of the analysis strategy of GEONET*." *Bull. Geogr. Surv. Inst* 49 (2003): 11-37.

[17] Urayasu City Government Homepage: http://www.city.urayasu.chiba.jp/, (accessed 25 September 2013).

[18] The Japanese Geotechnical Society, Japan Society of Civil Engineering, and Architectural Institute of Japan, "*Report of the Urayasu city review and research committee on liquefaction countermeasure techniques*", March 2012.

[19] Kanto Natural Gas Development Co Ltd., Abundant Reserves. http://www.gasukai.co.jp/english/gas/index4.html, (accessed 25 September 2013).

[20] Chiba Prefecture Homepage, http://www.pref.chiba.lg.jp/, (accessed 25 September 2013).

[21] Ferretti, A.; Prati, C.; Rocca, F., "*Nonlinear subsidence rate estimation using permanent scatterers in differential SAR interferometry*," *Geoscience and Remote Sensing, IEEE Transactions on*, vol.38, no.5, pp.2202,2212, Sep 2000.

[22] Colesanti, C.; Ferretti, A.; Novali, F.; Prati, C.; Rocca, F., "SAR monitoring of progressive and seasonal ground deformation using the permanent scatterers technique,"

*Geoscience and Remote Sensing, IEEE Transactions on*, vol.41, no.7, pp.1685,1701, July 2003.

[23] Monserrat, O.; Crosetto, M.; Cuevas, M.; Crippa, B., "The Thermal Expansion Component of Persistent Scatterer Interferometry Observations," *Geoscience and Remote Sensing Letters, IEEE*, vol.8, no.5, pp.864,868, Sept. 2011.

[24] S. Williams, Y. Bock, and P. Fang, "Integrated satellite interferometry: Tropospheric noise, GPS estimates and implications for interferometric synthetic aperture radar products," J. Geophys. Res., vol 103(B11), pp. 27051-27068, 1998.

[25] F. Onn and H. A. Zebker, "Correction for interferometric synthetic aperture radar atmospheric phase artifacts using time series of zenith wet delay observations from a GPS network," J. Geophys. Res., vol. 111, B09102, 16 pp, 2006.

[26] Li, Z., E. J. Fielding, P. Cross, and J.-P. Muller, "*Interferometric synthetic aperture radar atmospheric correction: Medium Resolution Imaging Spectrometer and Advanced Synthetic Aperture Radar integration*", *Geophys. Res. Lett., 33*. 2006.

[27] Li, Z., E. J. Fielding, P. Cross, and J.-P. Muller, "*Interferometric synthetic aperture radar atmospheric correction: GPS topography-dependent turbulence model*", *J. Geophys. Res., 111, 2006*.

[28] Doin M.-P., C. Lasserre, G. Peltzer, 0. Cavalié, C. Doubre, "*Corrections of stratified tropospheric delays in SAR interferometry: validation with global atmospheric models*", J. of Applied Geophysics, 69 (1), 2009.

[29] Löfgren, J.S.; Björndahl, F.; Moore, A. W.; Webb, F.H.; Fielding, E.J.; Fishbein, E.F., "*Tropospheric correction for InSAR using interpolated ECMWF data and GPS Zenith Total Delay from the Southern California Integrated GPS Network*," *Geoscience and Remote Sensing Symposium (IGARSS), 2010 IEEE International*, vol., no., pp.4503,4506, 25-30 July 2010.

[30] Walters, R. J., J. R. Elliott, Z. Li, and B. Parsons, "*Rapid strain accumulation on the Ashkabad fault (Turkmenistan) from atmosphere-corrected InSAR*", J. Geophys. Res. Solid Earth, 118,3674–3690. 2013.

[31] Hooper, "*A multi-temporal InSAR method incorporating both persistent scatterer and small baseline approaches*", Geophysical Research Letters 35, 2008.

[32] Ferretti, A.; Fumagalli, A.; Novali, F.; Prati, C.; Rocca, F.; Rucci, A., "*A New Algorithm for Processing Interferometric Data-Stacks: SqueeSAR*", *Geoscience and Rem*ote Sensing, IEEE Transactions on, vol.49, no.9, pp.3460,3470, Sept. 2011.

IntechOpen